

## Supporting Information

### **Artificial Bridge between Anode and Anolyte Enabled by Organic Ligand for Sustainable Zinc-Based Flow Batteries**

Liping Zhi,<sup>ab</sup>† Chenyi Liao,<sup>c</sup>† Pengcheng Xu,<sup>a</sup> Fusai Sun,<sup>bd</sup> Chenguang Yuan,<sup>a</sup> Fengtao Fan,<sup>d</sup> Guohui Li,<sup>\*c</sup> Zhizhang Yuan<sup>\*a</sup> and Xianfeng Li<sup>\*a</sup>

- a. Division of Energy Storage, Dalian National Laboratory for Clean Energy, Dalian Institute of Chemical Physics, Chinese Academy of Sciences, 457 Zhongshan Road, Dalian 116023, China. E-mail: yuanzhizhang@dicp.ac.cn; lixianfeng@dicp.ac.cn
- b. University of Chinese Academy of Sciences, Beijing 100049, China
- c. Laboratory of Molecular Modeling and Design, State Key Laboratory of Molecular Reaction Dynamics, Dalian Institute of Chemical Physics, Chinese Academy of Science, 457 Zhongshan Road, Dalian, 116023, China. Email: ghli@dicp.ac.cn
- d. State Key Laboratory of Catalysis, Dalian National Laboratory for Clean Energy, Collaborative Innovation Center of Chemistry for Energy Materials (iChEM), Dalian Institute of Chemical Physics, Chinese Academy of Sciences, 457 Zhongshan Road, Dalian 116023, China

† These authors contributed equally to this work

## Experimental Methods

**Materials:** Zinc oxide, sodium hydroxide, potassium hydroxide, sodium ferrocyanide, ethylenediaminetetraacetic acid (EDTA) were purchased from Tianjin Kemiou Chemical Reagent Co. Deuterated H<sub>2</sub>O (D<sub>2</sub>O) was bought from Aladdin-Holdings Group. These reagents were supplied with analytical grade.

**Battery Performance:** The alkaline zinc-iron flow battery (AZIFB) was assembled by using a polybenzimidazole (PBI) membrane between two carbon felt electrodes<sup>1</sup>, clamped by two graphite plates. The active area of the electrode is 6×8 cm<sup>2</sup>. All of these components were fixed between two stainless steel plates. The electrolyte was cyclically pumped through the corresponding electrodes in airtight pipelines. The cycling tests were conducted by ArbinBT 2000 at the constant current density of 80 mA cm<sup>-2</sup>. The rate performance was tested at the different charge/discharge current density ranging from 80 mA cm<sup>-2</sup> to 160 mA cm<sup>-2</sup>. The anolyte is made up of 80 mL of 0.4 mol L<sup>-1</sup> ZnO+ 3.8 mol L<sup>-1</sup> OH<sup>-</sup> with different EDTA concentration ranging from 0 to 0.7 mol L<sup>-1</sup>, the catholyte is made up of 80 mL of 0.8 mol L<sup>-1</sup> Fe(CN)<sub>6</sub><sup>4-</sup>+ 3 mol L<sup>-1</sup> OH<sup>-</sup>, unless otherwise specified. The charge process was controlled by the charge time to keep a constant charge capacity, while the discharge process was ended with a cut-off voltage of 0.1 V.

**Zn|Zn Symmetrical Flow Battery Test:** The Zn|Zn symmetrical flow battery was assembled by using zinc metal (6 cm×8 cm×0.06 cm) and carbon felt (6 cm×8 cm×0.42 cm, Liaoyang J-Carbon Materials Co., Ltd., China) as cathode, carbon felt (6 cm×8 cm×0.5 cm) as anode. 160 mL of 0.4 mol L<sup>-1</sup> ZnO in 3.8 mol L<sup>-1</sup> OH<sup>-</sup> with or without EDTA solution was used as catholyte and anolyte. The test was carried out by plating a given amount of Zn metal onto the carbon felt substrate, followed by stripping Zn metal from the carbon felt substrate with a cut-off voltage (-0.5 V).

**Chronoamperometry Test:** Chronoamperometry (CA) was carried out by applying an initial potential at -1.445 V vs. Hg/HgO employing a three-electrode cell with a glassy carbon working electrode a Hg/HgO reference electrode and a graphite plate counter electrode, for investigation the nucleation way of zinc ions. An initial potential of -1.67 V vs. Hg/HgO was applied with a rotation rate of 200 rpm to investigate the plating behavior of zinc ions. Notably, the experiment of CA was further carried out using Zn|Zn symmetrical flow battery at the overpotential of -100 mV for researching the diffusion model of zinc ions. All the experiments of CA were tested using 0.4 mol L<sup>-1</sup> ZnO+ 3.8 mol L<sup>-1</sup> OH<sup>-</sup> solution with different concentrations of EDTA ranging from 0 to 0.3 mol L<sup>-1</sup>.

**The AZIFB Cell Stack:** A hundred-watt level cell stack consisting of 10 single cells was assembled to confirm the practicality of the anolyte. 30 L of 0.4 mol L<sup>-1</sup> EDTA+ 0.6 mol L<sup>-1</sup> ZnO+ 5.2 mol L<sup>-1</sup> OH<sup>-</sup> and 30 L of 0.8 mol L<sup>-1</sup> Fe(CN)<sub>6</sub><sup>4-</sup>+ 0.8 mol L<sup>-1</sup> OH<sup>-</sup> were used as anolyte and catholyte, respectively. The effective electrode area of each single cell was 1000 cm<sup>2</sup>. The single cell consists of two carbon felt electrodes separated by a PBI membrane, a homemade carbon-plastic bipolar plate, PVC frames and gaskets.

**Electrochemical Measurements:** Rotating disk electrode (RDE) was performed on a Gamry Multichannel System installation (Reference 3000) employing a three-electrode cell with a graphite plate working electrode (2 cm<sup>2</sup>) (a glassy carbon electrode with an effective area of 0.1963 cm<sup>2</sup> was used as the working electrode), a Hg/HgO reference electrode and a graphite plate counter electrode. Different kinds of anolytes were employed for RDE tests: 0.1 mol L<sup>-1</sup> ZnO+ 3.2 mol L<sup>-1</sup> OH<sup>-</sup> with different EDTA concentration ranging from 0 to 0.075 mol L<sup>-1</sup> at room temperature. The RDE experiment was measured from -1.35 V to -1.68 V versus Hg/HgO at a sweep rate of 10 mV s<sup>-1</sup> with rotation rate ranging from 100 rpm to 500 rpm. The RDE experiments were conducted at room temperature. The viscosity of the electrolyte is measured by a Kinematic viscometer (GB/T-265). The limiting currents were plotted versus the rotation rate. The diffusion coefficient (D<sub>0</sub>) of zinc ion/Zn redox couple was fit using the Levich equation<sup>2</sup>:  $i_{Lim}=0.62nFAD_0^{2/3}\omega^{1/2}\nu^{-1/6}C$ , where the  $i_{Lim}$  is limiting current, n is the number of electrons transferred (n=2), F is Faradaic constant (96485 C mol<sup>-1</sup>), A is the surface area of the working electrode (0.1963 cm<sup>2</sup>), C is the concentration of redox species (1.0 ×10<sup>-4</sup> mol cm<sup>-3</sup>),  $\omega$  is the rotation rate (rad s<sup>-1</sup>) and  $\nu$  is the kinetic viscosity (mm<sup>2</sup> s<sup>-1</sup>). The exchange current was calculated using the Koutecky-Levich equation<sup>3</sup>:

$$\frac{1}{i} = \frac{1}{i_k} + \frac{1}{i_L} = \frac{1}{i_k} + \frac{1}{0.62nFAD_0^{2/3}\omega^{1/2}\nu^{-1/6}C} \quad (1)$$

The exchange current  $i_0$  can be obtained by fitting current  $i_k$  to the Tafel plot at the overpotential of zero, from which the reaction rate constant  $k_0$  can be calculated according to Butler-Volmer equation<sup>4</sup>:  $i_0 = nFCAk_0$ .

Cyclic voltammetry (CV) was performed on a Gamry Multichannel System installation (Reference 3000) employing a three-electrode cell with a graphite plate working electrode (2 cm<sup>2</sup>) (a glassy carbon electrode with an effective area of 0.1963 cm<sup>2</sup> was used as the working electrode), a Hg/HgO reference electrode and a graphite plate counter electrode. Different kinds of anolytes were employed for CV tests: 0.4 mol L<sup>-1</sup> ZnO + 3.8 mol L<sup>-1</sup> OH<sup>-</sup> + 0.3 mol L<sup>-1</sup> EDTA at a sweep rate from 10 mV s<sup>-1</sup> to 60 mV s<sup>-1</sup> with rotation rate of 0 rpm or 500 rpm, respectively.

Hydrogen evolution reaction (HER) potential was performed by linear sweep voltammetry (LSV) at a potential from -1.85 V to -2.15 V on a Gamry Multichannel System installation (Reference 3000) employing a three-electrode cell with a graphite plate working electrode (2 cm<sup>2</sup>) (a glassy carbon electrode with an effective area of 0.1963 cm<sup>2</sup> was used as the working electrode), a Hg/HgO reference electrode and a graphite plate counter electrode. Different kinds of anolytes were employed for LSV tests: 0.1 mol L<sup>-1</sup> ZnO + 3.2 mol L<sup>-1</sup> OH<sup>-</sup> with different EDTA concentration ranging from 0 to 0.175 mol L<sup>-1</sup> at room temperature.

**Zinc Metal Morphologies:** The field emission scanning electron microscopy (FE-SEM, JEOL 6360LV, Japan) was employed to characterize the morphologies of the zinc metal deposited on the carbon felt at the end of AZIFB (with/without EDTA) charging process.

**TOF-MS measurements:** Time-of-flight mass spectrometry (TOF-MS, M6, IONTOF GmbH) was employed to characterize the spatially distributed state of metallic zinc deposited on the carbon felt at the end of AZIFB charging process by three-dimensional imaging and depth analysis using argon gas in a gas cluster ion beam with 2 Kev.

**Characterization:** NMR was carried out on a Bruker AVANCE III HD 400MHz equipment (Germany) to illustrate the <sup>1</sup>H and <sup>13</sup>C bonds changes in various EDTA-containing electrolytes. A liquid sample with a volume of about 400 μL was prepared via the coaxial double tube where the inner tube was filled with deuterated reagent and the outer tube was filled with the sample. The deuterated reagent was used as the field frequency lock for NMR tests. Deuterated H<sub>2</sub>O (D<sub>2</sub>O), a common reagent, was used at room temperature for NMR test, unless otherwise specified. Solid state <sup>67</sup>Zn NMR analysis was carried out on a Bruker AVANCE III HD 600MHz equipment (Germany) to illustrate the <sup>67</sup>Zn bonds changes in various electrolytes. Thermo Fisher FTIR spectrometer (Thermo Fisher, Nicolet iS50) was used to record different solutions and electrodes (electrode was soaked over 72 hours in 0.4 mol L<sup>-1</sup> ZnO+ 3.8 mol L<sup>-1</sup> OH<sup>-</sup> solution with different concentration of EDTA ranging from 0 to 0.7 mol L<sup>-1</sup>) from 4000 to 400 cm<sup>-1</sup> in transmission mode. It is worth noting that the diamond window is used for the solution and the potassium bromide pressing method is used for the electrode. The X-ray diffraction (XRD) patterns were performed using an X-ray diffractometer (D8 ADVANCE ECO; RIGAKU, Japan). X-ray photoelectron spectrometer (XPS, Thermofisher Escalab 250 xi+) was employed to detect the element distribution on anode after soaking it in 0.4 mol L<sup>-1</sup> ZnO + 3.8 mol L<sup>-1</sup> OH<sup>-</sup> solution with different concentration of EDTA ranging from 0 to 0.7 mol L<sup>-1</sup> for over 72 hours.

**In situ AFM measurements:** Highly oriented pyrolytic graphite (HOPG) was used as the working electrode, and Zn wire was used as the counter electrode and the reference electrode. Electrochemical deposition was conducted on the CHI760E workstation at a current density of 5 mA cm<sup>-2</sup> using solution consisting of 0.4 mol L<sup>-1</sup> ZnO+ 3.8 mol L<sup>-1</sup> OH<sup>-</sup> with different EDTA concentration ranging from 0 to 0.3 mol L<sup>-1</sup>. In situ topographical imaging (PeakForce tapping Mode) of Zn in liquid was performed using commercial SCANASYST-FLUID+ probe on Dimension ICON atomic force microscope (Bruker). The optical images were taken with Bruker's own optical microscope. The height information was analyzed by Nanoscope analysis software.

**Numerical Simulation:** A three-dimensional homeostatic model of full battery using 0.4 mol L<sup>-1</sup> ZnO + 3.8 mol L<sup>-1</sup> OH<sup>-</sup> without EDTA or with 0.3 mol L<sup>-1</sup> EDTA as anolyte and using 0.8 mol L<sup>-1</sup> Fe(CN)<sub>6</sub><sup>4-</sup> + 3 mol L<sup>-1</sup> OH<sup>-</sup> as catholyte was constructed to

simulate the effect of EDTA on the distribution of zinc species' concentration and overpotential inside an alkaline zinc-iron flow battery. In the calculation model, the cubic current distribution was employed to guarantee the momentum transfer and mass transfer of each ion in the battery, and the flow of electrolyte in porous electrode was governed by linear Darcy's law physical field. The velocity and pressure were set as the entrance and outlet boundary conditions of the electrode, respectively. The boundary conditions for the 3D homeostatic full battery model are as follows: the inlet velocity is  $0.03 \text{ m s}^{-1}$  in the normal direction of flow, and the outlet pressure is 101325 Pa. Darcy's law describes the linear relationship between velocity field and pressure gradient. The linear Darcy's law is suitable for describing the low velocity flow in porous materials with Reynolds number less than 10. The expression of linear is as follows:

$$u = -(k/\mu)\nabla p$$

where  $u$ ,  $k$ ,  $\mu$  and  $\nabla p$  represent the velocity, permeability of the porous material, the dynamic viscosity of the fluid, and pressure gradient of the fluid, respectively.

In the regular structure (regular porous carbon electrodes are used in our simulations and experiments), the permeability of  $k$  can be deduced from the Kozeny-Carman relation.

$$k = \psi^3 / [c(1-\psi)^2 S^2]$$

where  $\psi$  is the porosity of porous material. And  $c$  and  $S$  are Kozeny-Carman constant of 4.28 and specific surface area of solid phase, respectively

The working current density of the battery is  $40 \text{ mA cm}^{-2}$ . The structure of the battery and composition of anolyte are consistent with the actual battery measurement (the section of battery performance). The model was solved by using commercial COMSOL based on multi-physical field coupling calculation and solver of PARSISO. The relative error tolerance was set to 0.001. The viscosity, density, conductivity for anolyte without EDTA are  $2.33 \text{ mPa}\cdot\text{s}$ ,  $1.18 \text{ g mL}^{-1}$ ,  $297 \text{ mS cm}^{-1}$ , respectively, while the viscosity, density, conductivity for anolyte with  $0.3 \text{ mol L}^{-1}$  EDTA are  $2.64 \text{ mPa}\cdot\text{s}$ ,  $1.18 \text{ g mL}^{-1}$ ,  $245 \text{ mS cm}^{-1}$ , respectively. These parameters including anolyte properties (viscosity, density, conductivity), charge numbers of EDTA- $\text{Zn}(\text{OH})_3^-$  and  $\text{Zn}(\text{OH})_4^{2-}$  are different and considered during the simulation process.

**Molecular dynamics (MD) simulations of  $\text{Zn}^{2+}$  anolyte.** We applied MD simulations to investigate the influence of EDTA with different concentrations on zinc ion solvation structure. All MD simulations were performed with the general AMBER force field (GAFF)<sup>5</sup>. The force field parameters for EDTA and  $\text{OH}^-$  were computed at the HF/6-31G\* level of theory by performing Gaussian g09<sup>6</sup> calculations. Then, antechamber was used to assign the GAFF parameters, calculate the restricted electrostatic potential (RESP) under Gaussian g09, and create the AMBER PREP files for EDTA and  $\text{OH}^-$ , respectively. The force field parameters for  $\text{OH}^-$  were modified on the 12-6 Lennard-Jones (LJ) parameters to better describe aqueous solutions (Table S1). We constructed a  $60 \times 60 \times 60 \text{ \AA}^3$  box that contains EDTA,  $\text{Zn}^{2+}$ ,  $\text{OH}^-$ , SPC/E model  $\text{H}_2\text{O}$ , and  $\text{Na}^+$  according to different electrolyte formula (Table S2) using PACKMOL<sup>7</sup> and further processed using LEaP in AMBER18 package<sup>8</sup>.

Each system went through energy minimization, 125 ps isothermal-isovolumetric (NVT) ensemble with position restraint on solute components. Then, the system continued to relax without restraint under isothermal-isotropic (NPT) ensemble using the AMBER18 package<sup>8</sup> with GPU acceleration. The NPT ensemble was set with 298 Kelvin, 1 bar, Langevin dynamics thermostat and a time step of 2 fs. All lengths of bonds to hydrogen atoms in solute components were constrained with SHAKE. The particle mesh Ewald (PME) technique was used for the electrostatic calculations. The van der Waals and short-range electrostatics were cut off at  $12.0 \text{ \AA}$  with switch at  $10.0 \text{ \AA}$ . Each system was simulated with three 4000-ns MD simulation replicas. Data analysis was performed with either "cpptraj"<sup>9</sup> and further processed and plotted using matplotlib<sup>10</sup>. Structural features were shown by Pymol (Schrödinger, LLC). A summary of MD simulations is provided in Table S2.

**Molecular simulations of solvated  $\text{Zn}^{2+}$  on graphene.** We applied MD simulations to obtain the adsorbed configurations of  $\text{Zn}^{2+}/\text{OH}^-/\text{EDTA}$  complex and  $\text{Zn}(\text{OH})_4^{2-}$  on graphene surface in aqueous environment. The [001] surface of graphene (unit cell parameters as  $2.46 \text{ \AA}$ ,  $2.46 \text{ \AA}$ ,  $6.8 \text{ \AA}$  and cell angle of  $90^\circ$ ,  $90^\circ$ ,  $120^\circ$ ) was cleaved using Material Studio 6.0 (Accelrys, Inc.). Rectangular graphene unit cell was generated and constructed into  $6 \times 7 \times 1$  supercell ( $29.52 \times 29.82 \times 3.4 \text{ \AA}^3$ ). Topology of

graphene was generated by gmx x2top with the Oplsaa-based force field parameters for Carbon Nanotubes and graphene by Andrea Minoia (<http://chembytes.wikidot.com/grocnt>)<sup>11</sup>. First, we extract the [EDTA·Zn(OH)<sub>3</sub>]<sup>5-</sup> and Zn(OH)<sub>4</sub><sup>2-</sup> structures from MD simulations of Zn-EDTA system under 0.3 M EDTA, which were solvated with SPC/E model H<sub>2</sub>O in periodic box of 27×27×27 Å<sup>3</sup> using LEaP in AMBER18 package<sup>8</sup>. The Zn<sup>2+</sup>/OH<sup>-</sup>/EDTA and Zn(OH)<sub>4</sub><sup>2-</sup> systems were added with three Zn<sup>2+</sup> and one OH<sup>-</sup> or one Zn<sup>2+</sup> as counter ions, respectively. The AMBER inputs of the solvated box are converted into GROMACS inputs using amb2gro\_top\_gro.py program, then combined with the structure and force field of graphene surface. The whole Zn<sup>2+</sup>-complex-on-graphene systems contain 518~559 water molecules, totaling 1934~2016 atoms in periodic box of 29.52×29.82×34 Å<sup>3</sup>.

The system went through energy minimization, 125 ps equilibration with timestep of 1 ps under isothermal-isovolumetric (NVT) ensemble, then continued to relax with time step of 2 ps under NVT (298 K, v-rescale temperature coupling) using the GROMACS 2019.4 package<sup>12</sup>. The position of graphene is restrained during MD simulations. The particle mesh Ewald (PME) technique<sup>13</sup> was used to calculate long-range electrostatic interactions. The van der Waals and short-range electrostatics were cut off at 12.0 Å with switch at 10.0 Å. Each system was simulated with two 200 ns MD simulation replicas. Eventually, the [Zn<sub>2</sub>(OH)<sub>4</sub>EDTA]<sup>4-</sup> are formed and adsorb on the graphene in Zn<sup>2+</sup>/OH<sup>-</sup>/EDTA system.

**First-principles density functional theory (DFT) calculations.** We generated eleven adsorbed configurations of Zn<sup>2+</sup> complex (in explicit solvent environment) from the last 100 ns of each MD simulation (totaling 22 explicit-solvent configurations each system) for adsorption energy calculations, projected density of states (PDOS), and charge density difference analysis. These configurations were further processed to remove all the bulk solvent molecules and keep only the adsorbed Zn complex with the first solvation shell and graphene. All DFT calculations are carried out using the Quickstep module of the CP2K program suite<sup>14</sup>. In Quickstep, a dual basis of localized Gaussians and plane waves (GPW) is used to represent the Kohn-Sham equation and electronic density<sup>15</sup>. We used DZVP-MOLOPT-GTH (valence double- $\zeta$  plus polarization, molecularly optimized, Goedecker-Teter-Hutter<sup>16</sup>) basis set for C, H, O, N atoms and DZVP-MOLOPT-SR-GTH basis set for Zn. Periodic boundary conditions were employed for the system of 29.52×29.82×84 Å<sup>3</sup> with vacuum slab more than 70 Å along the z axis. After a convergence scanning in planewave cutoff, we use cutoff of 500 Ry with REL\_CUTOFF of 60 Ry. The Perdew–Burke–Erzerhof (PBE)<sup>17</sup> exchange correlation functional is used. Dispersion interactions were included using the Grimme’s D3 correction<sup>18</sup> within a range of 15 Å. The orbital transformation (OT) method is used in the self-consistent field (SCF) wavefunction optimization cycle.

The charge density difference induced by adsorption of different Zn complexes are computed by subtracting the charge densities of the lone graphene and adsorbate from the adsorbed system using the cubecruncher tool of CP2K<sup>14</sup>. The adsorption energy is calculated by  $E_{\text{adsorbed}} = E_{\text{system}} - E_{\text{adsorbate}} - E_{\text{surface}}$ . Similarly, the energy of a OH<sup>-</sup> or the whole Zn-OH cluster to dissociate from the adsorbed Zn(OH)<sub>4</sub><sup>2-</sup> or [EDTA·Zn(OH)<sub>3</sub>·Zn·H<sub>2</sub>O]<sup>4-</sup> complex on graphene is calculated by  $E_{\text{dissociated}} = E_{\text{group a}} + E_{\text{group b}} - E_{\text{group a+b}}$ . The adsorption and dissociation energies are calculated over 22 configurations, and the strongest adsorption energy configurations are displayed in Fig 3a and 3b. The PDOS outputs were processed using two python scripts (available at [http://wiki.wpi.edu/deskinsgroup/Density\\_of\\_States](http://wiki.wpi.edu/deskinsgroup/Density_of_States)) to do the convolution. The PDOS of different components were averaged over 22 configurations of 200 ns to obtain a representative ensemble average. The p-band center is defined as the centroid of the PDOS of the 2p orbitals relative to the Fermi level by the formula:

$$E_{\text{center}} = \frac{\int_{-\infty}^a E \cdot pdos(E) dE}{\int_{-\infty}^a pdos(E) dE} - E_{\text{Fermi}}$$

Where  $pdos(E)$  and  $E$  are projected density of states and energy of 2p states. We chose the  $[-\infty, 5]$  width for graphene and  $[-\infty, 3]$  for the rest components.

**Table S1** Nonbonded parameters used for OH<sup>-</sup> in this study.

Atom	$r_{\min}/2$ (Å) <sup>a</sup>	epsilon (kcal mol <sup>-1</sup> )	q (e)
O (OH)	1.98	0.1	-1.2
H (OH)	0	0	0.2

<sup>a</sup>  $r_{\min}$  is the distance of two atoms at Lennard-Jones potential minimum.

**Table S2** A summary of simulations.

System	atom No.	EDTA	OH <sup>-</sup>	H <sub>2</sub> O	Na <sup>+</sup>	Zn <sup>2+</sup>	simulation time (ns)
Blank	2680	0	230	2240	190	20	4000×3
0.3 EDTA	7030	15	150	2020	170	20	4000×3
0.7 EDTA	7750	35	150	2020	250	20	4000×3

## Results and Discussion

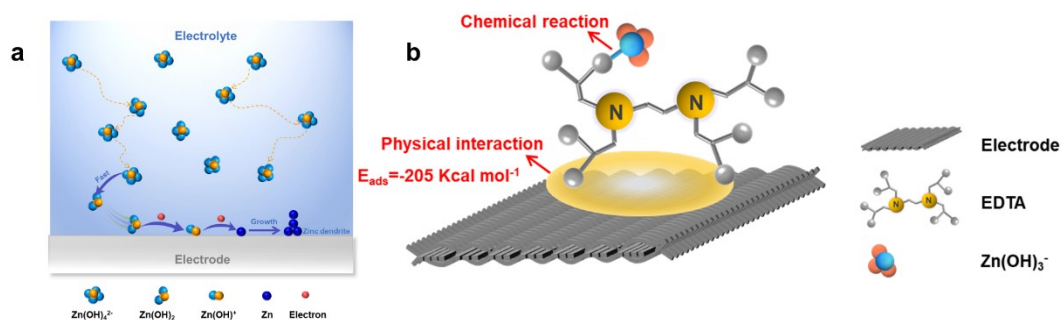
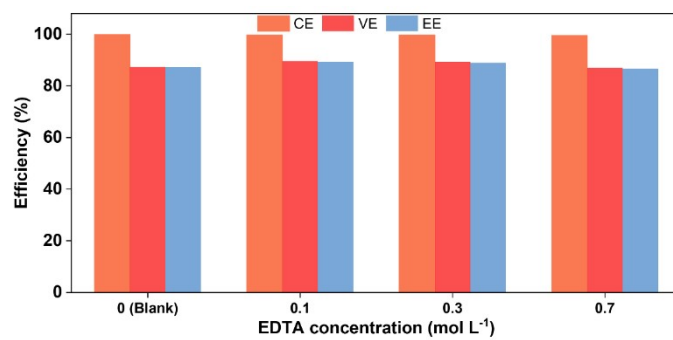
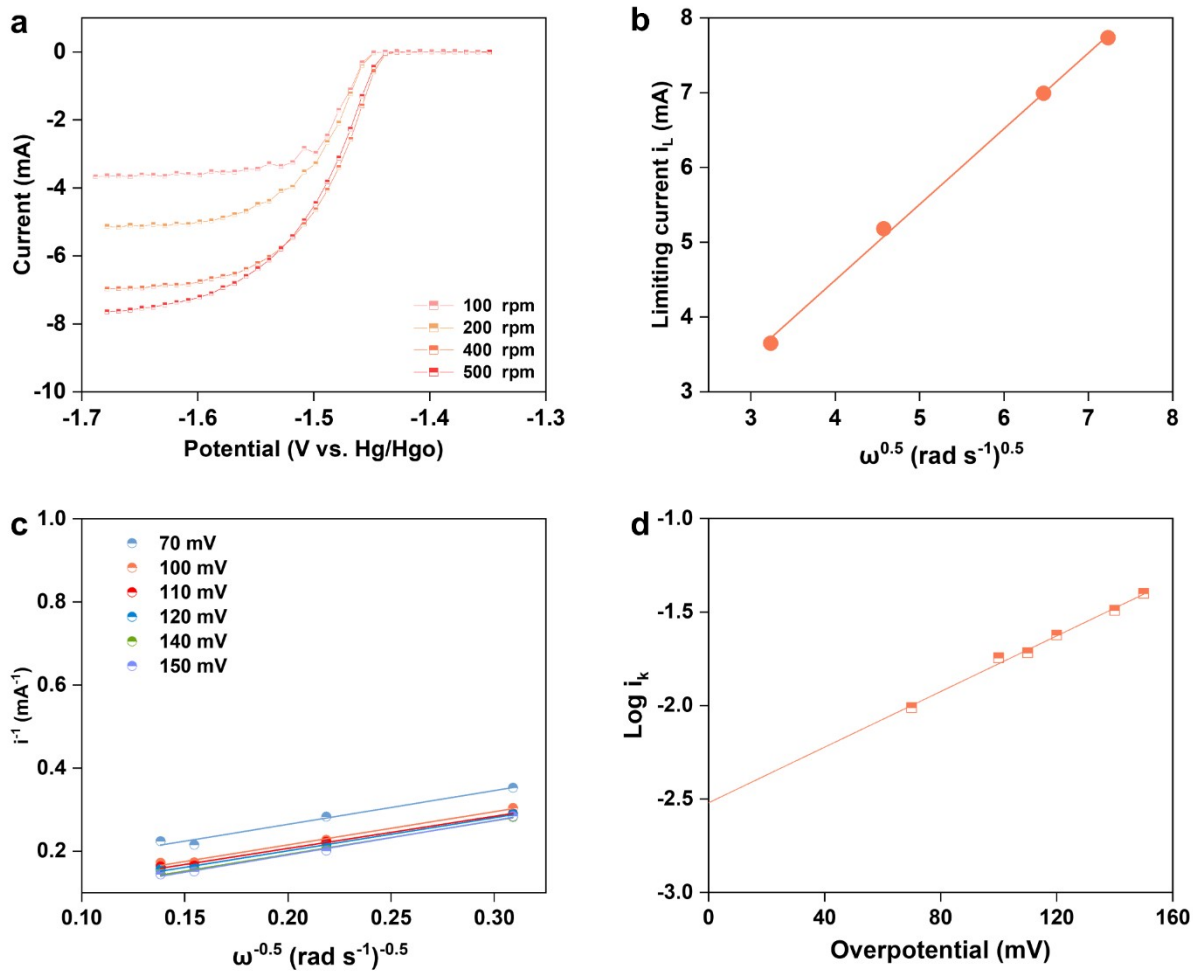


Fig.S1 (a) Schematic diagram of zincate ions ( $\text{Zn(OH)}_4^{2-}$ ) deposition process in alkaline solution. (b) Schematic illustration of the role of artificial bridge in plating process of  $\text{EDTA}\cdot\text{Zn(OH)}_3^-$ .

In traditional anolyte ( $\text{Zn(OH)}_4^{2-}$  in alkaline solution) for alkaline zinc-iron flow battery, when the battery is charging, the zincate ions diffuse from the bulk solution to surface of anode and experience a desolvation process. The desolvated zincate ions then adsorb on anode and obtain two electrons to be reduced to zinc metal (Fig.S1a). The plating of zincate ion is a mass transfer control process, which results in a poor concentration of active material on surface of anode and further a concentration polarization on the electrode. This makes the plating of zincate ions in a direction opposite that of their diffusion path. Thus, compared with other region of the electrode, the zincate ions are more favored to diffuse into those protruding points to deposition, with the formation of dendrite zinc. While in anolyte containing EDTA ligand, EDTA first coordinates with  $\text{Zn(OH)}_4^{2-}$  to form  $\text{EDTA}\cdot\text{Zn(OH)}_3^-$  via the coordination of zinc ion with three  $\text{OH}^-$  and one carboxyl oxygen from EDTA, and then adsorbs on surface of anode via the physical interaction (Fig.S1b). The adsorption of  $\text{EDTA}\cdot\text{Zn(OH)}_3^-$  cause its band center to move toward the Fermi surface, leading to enhanced adsorption capacity and charge migration at the interface. Thus, we see the EDTA ligand that bridges the zinc species and the anode at the anolyte-anode interface as the artificial bridge, which facilitates the directional transport of zinc species, further promoting their efficient and controlled movement towards the anode. To clarify this, more discussion was added in the revised version.



**Fig.S2** The performance (10<sup>th</sup>) of alkaline zinc-iron flow battery at the current density of 80 mA cm<sup>-2</sup> using 0.4 mol L<sup>-1</sup> ZnO+ 3.8 mol L<sup>-1</sup> OH<sup>-</sup> anolyte with different concentration of EDTA ranging from 0 to 0.7 mol L<sup>-1</sup>.



**Fig.S3** (a) Rotating disk electrode (RDE) experiment. (b) Fitted linear Levich plots of the limiting current ( $i_{\text{Lim}}$ ) versus the square root of rotation rate ( $\omega^{0.5}$ ). (c) Linearly fitted Koutecky-Levich plots of  $i^{-1}$  with respect to  $\omega^{-0.5}$ . (d) Linearly fitted plots of  $\log i_{\text{k}}$  at different overpotentials for rotating disk electrode.  $0.1 \text{ mol L}^{-1} \text{ ZnO} + 3.2 \text{ mol L}^{-1} \text{ OH}^-$  solution was employed.

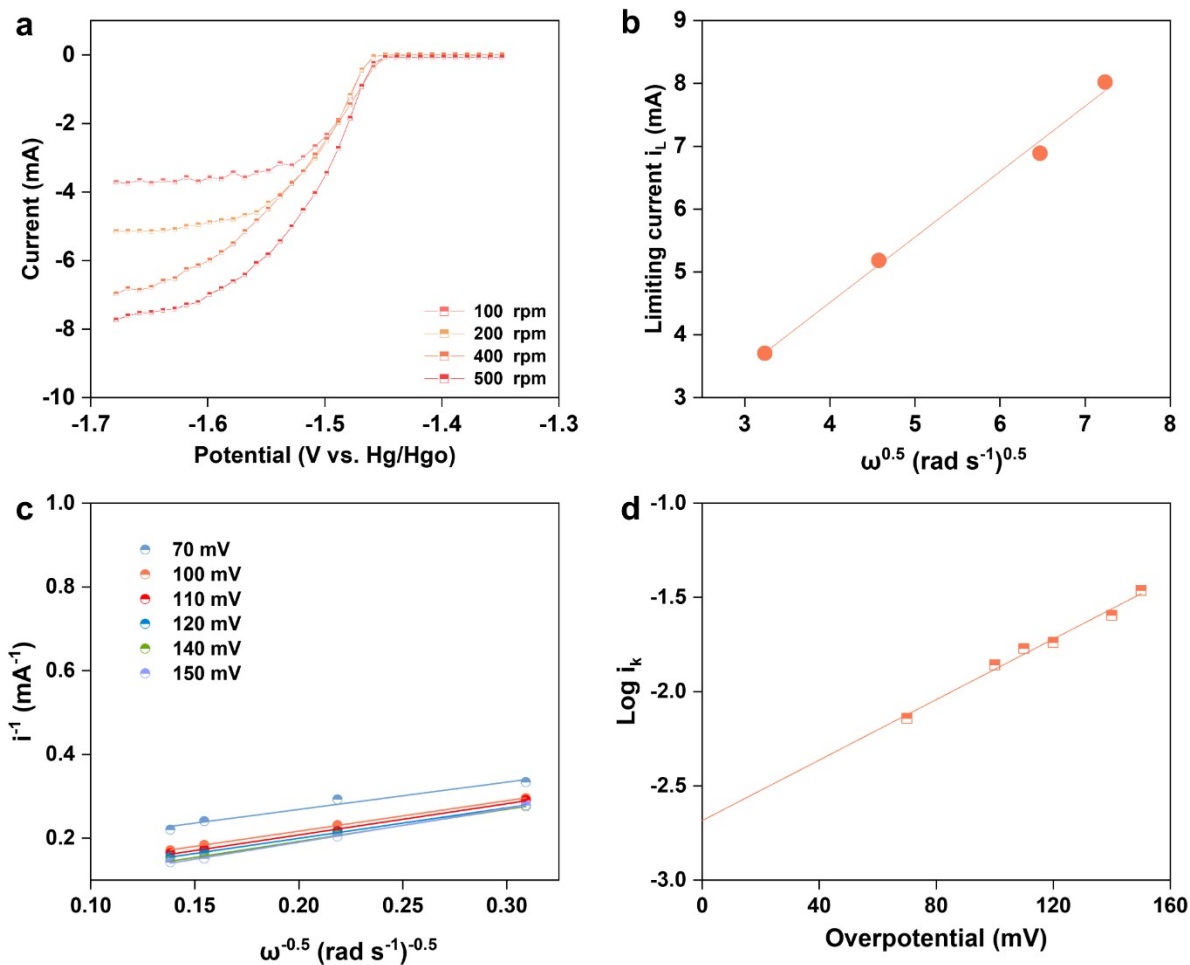


**Fig.S4** (a) Rotating disk electrode (RDE) experiment. (b) Fitted linear Levich plots of the limiting current ( $i_{Lim}$ ) versus the square root of rotation rate ( $\omega^{0.5}$ ). (c) Linearly fitted Koutecky-Levich plots of  $i^{-1}$  with respect to  $\omega^{-0.5}$ . (d) Linearly fitted plots of log  $i_k$  at different overpotentials for rotating disk electrode. 0.1 mol L<sup>-1</sup> ZnO + 3.2 mol L<sup>-1</sup> OH<sup>-</sup> + 0.075 mol L<sup>-1</sup> EDTA solution was employed.

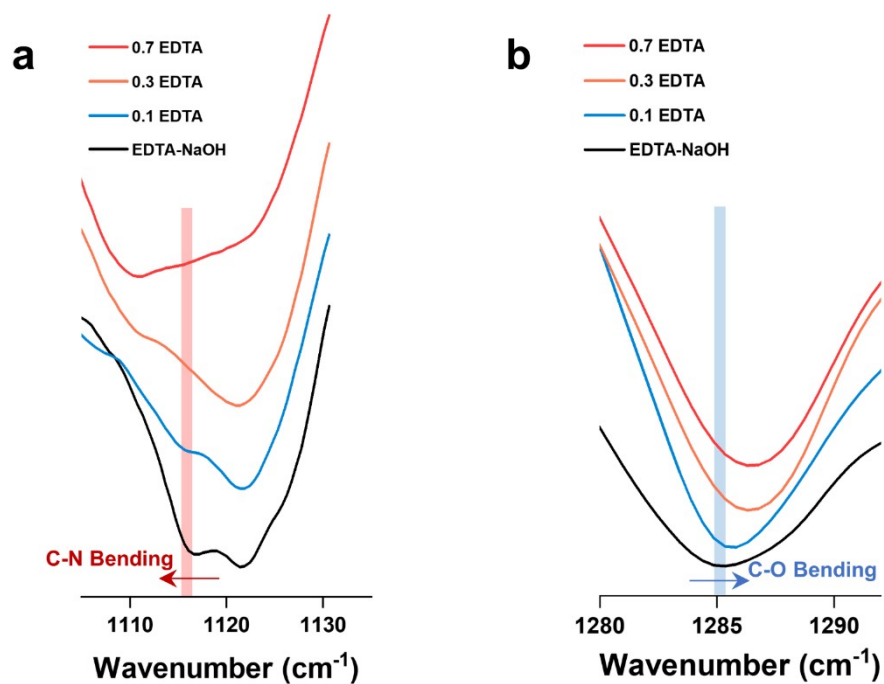


**Fig.S5** (a) and (b) The FTIR spectra of EDTA in sodium hydroxide solution (abbreviated as EDTA-NaOH) and 0.4 mol L<sup>-1</sup> ZnO + 3.8 mol L<sup>-1</sup> OH<sup>-</sup> solution with different concentration of EDTA ranging from 0.1 to 0.7 mol L<sup>-1</sup> (abbreviated as 0.1 EDTA, 0.3 EDTA, 0.7 EDTA, respectively).

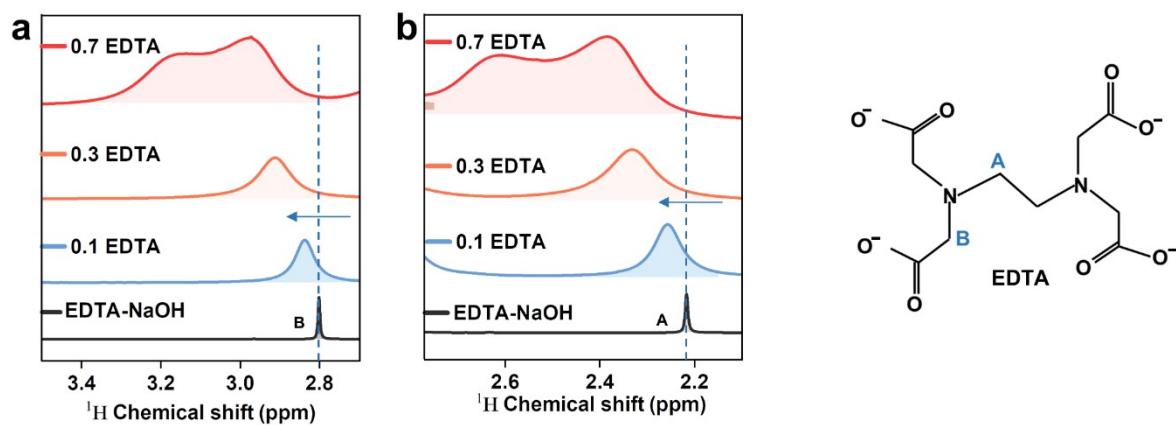


**Fig.S6** (a) and (b) The  $^1\text{H}$  NMR spectra of EDTA in sodium hydroxide solution (abbreviated as EDTA-NaOH) and  $0.4 \text{ mol L}^{-1} \text{ ZnO}$  +  $3.8 \text{ mol L}^{-1} \text{ OH}^-$  solution with different concentration of EDTA ranging from 0.1 to 0.7  $\text{mol L}^{-1}$  (abbreviated as 0.1 EDTA, 0.3 EDTA, 0.7 EDTA, respectively).

The chemical shift was corrected by chemical shift of water. The chemical structural formula of EDTA on the far right.

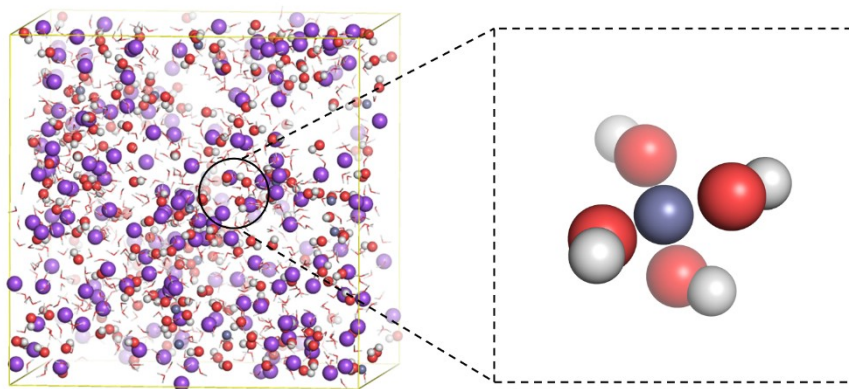


**Fig.S7** Molecular dynamics equilibrium state from MD simulations and the magnified snapshot representing the solvated structure of zinc ion in  $0.4 \text{ mol L}^{-1} \text{ ZnO} + 3.8 \text{ mol L}^{-1} \text{ OH}^-$  solution.

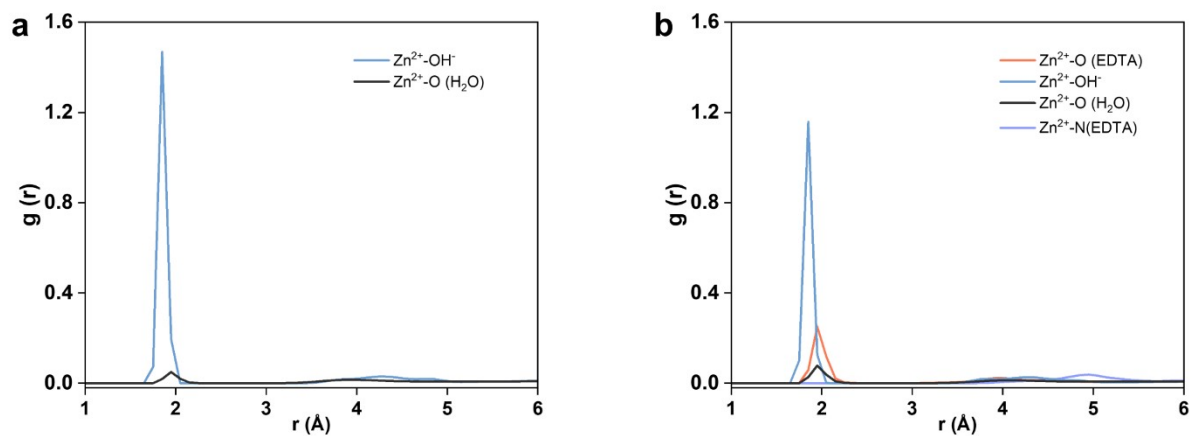


**Fig.S8** Radial distribution function  $g(r)$  of different components as a function of distance from  $Zn^{2+}$  in (a)  $0.4 \text{ mol L}^{-1} \text{ ZnO} + 3.8 \text{ mol L}^{-1} \text{ OH}^-$  solution and (b)  $0.4 \text{ mol L}^{-1} \text{ ZnO} + 3.8 \text{ mol L}^{-1} \text{ OH}^- + 0.7 \text{ mol L}^{-1} \text{ EDTA}$  solution. The bulk water  $g(r)$  as 1 is used as reference.

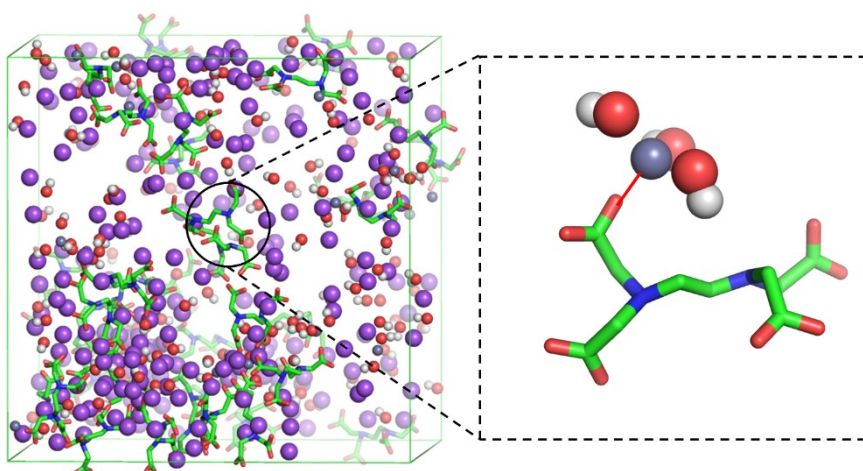


**Fig.S9** Molecular dynamics equilibrium state from MD simulations and the magnified snapshot representing the solvated structure of zinc ions in  $0.4 \text{ mol L}^{-1} \text{ ZnO} + 3.8 \text{ mol L}^{-1} \text{ OH}^- + 0.7 \text{ mol L}^{-1} \text{ EDTA}$  solution.

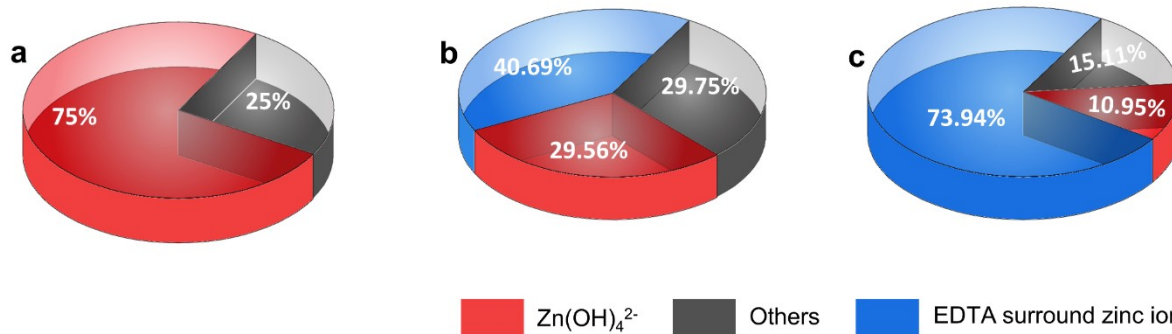


**Fig.S10** Distribution of EDTA and OH<sup>-</sup> participating in zinc ion solvation structure in 0.4 mol L<sup>-1</sup> ZnO + 3.8 mol L<sup>-1</sup> OH<sup>-</sup> solution with (a) 0, (b) 0.3 mol L<sup>-1</sup>, and (c) 0.7 mol L<sup>-1</sup> EDTA.

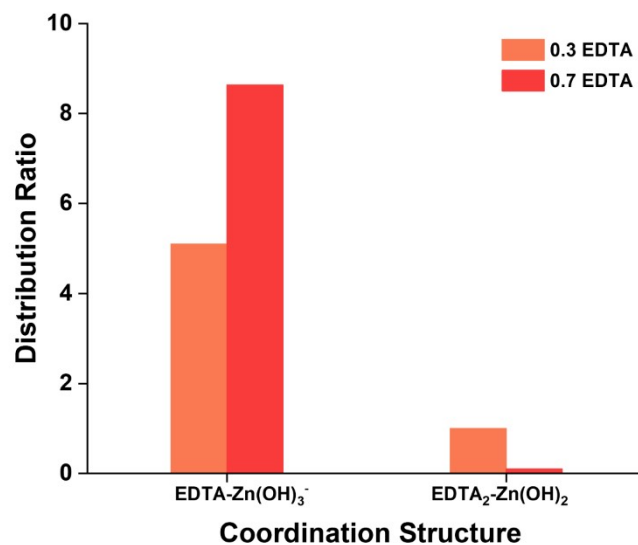


**Fig.S11** The coordination structure of EDTA surrounded zinc ion. The number of molecules of EDTA<sub>2</sub>-Zn(OH)<sub>2</sub> in 0.4 mol L<sup>-1</sup> ZnO + 3.8 mol L<sup>-1</sup> OH<sup>-</sup> anolyte with 0.3 mol L<sup>-1</sup> EDTA is used as a reference for normalization.

EDTA surround zinc ion comprises EDTA-Zn(OH)<sub>3</sub><sup>-</sup> and EDTA<sub>2</sub>-Zn(OH)<sub>2</sub>, while the presence of EDTA-Zn(OH)<sub>2</sub>, and EDTA-Zn(OH)<sup>+</sup> has not been observed. Furthermore, with increasing concentration of EDTA in anolyte, the proportion of EDTA-Zn(OH)<sub>3</sub><sup>-</sup> ions gradually increases, as illustrated in the Fig.S11.

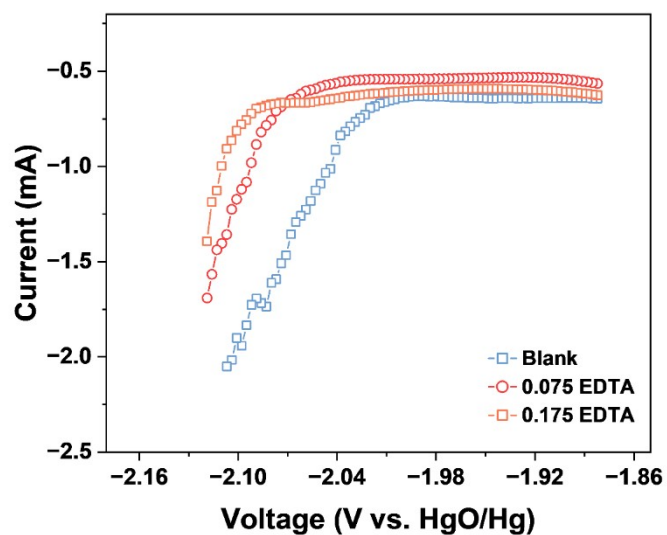


**Fig.S12** The HER potentials of 0.1 mol L<sup>-1</sup> ZnO + 3.2 mol L<sup>-1</sup> OH<sup>-</sup> analyte with different EDTA concentrations using a glassy carbon as working electrode at a scanning rate of 1 mV s<sup>-1</sup>.

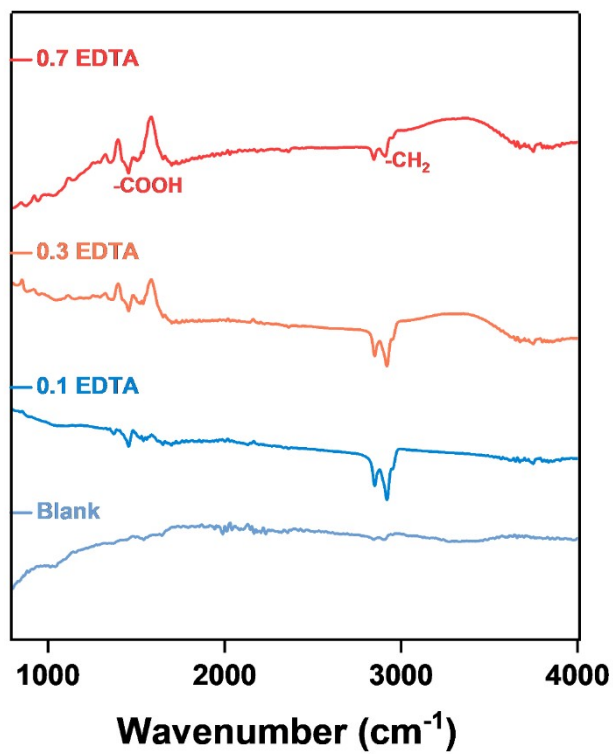


**Fig.S13** The FTIR spectra of carbon electrode soaked in 0.4 mol L<sup>-1</sup> ZnO + 3.8 mol L<sup>-1</sup> OH<sup>-</sup> solution with different concentration of EDTA ranging from 0 to 0.7 mol L<sup>-1</sup> for over 72 hours.

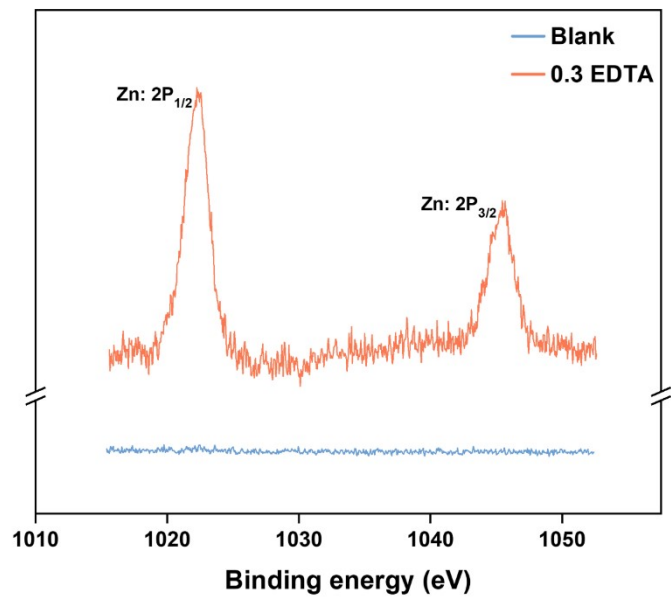


**Fig.S14** The XPS spectra of carbon electrode soaked in  $0.4 \text{ mol L}^{-1} \text{ ZnO} + 3.8 \text{ mol L}^{-1} \text{ OH}^-$  without/with  $0.3 \text{ mol L}^{-1} \text{ EDTA}$  solution for over 72 hours.

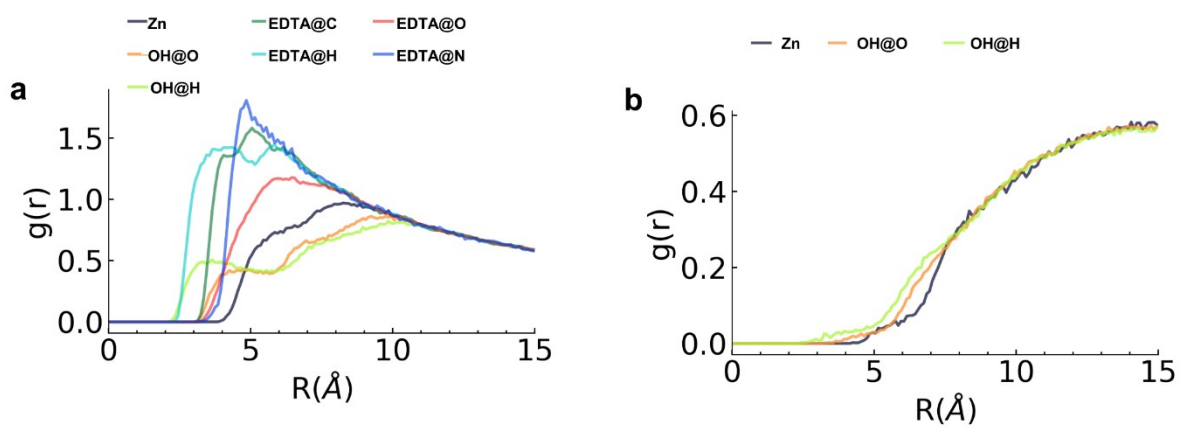


**Fig.S15** Radial distribution function  $g(r)$  of different components as a function of (a) adsorbed  $\text{EDTA}\cdot\text{Zn}(\text{OH})_3^-$  and (b)  $\text{Zn}(\text{OH})_4^{2-}$  distance from graphene.

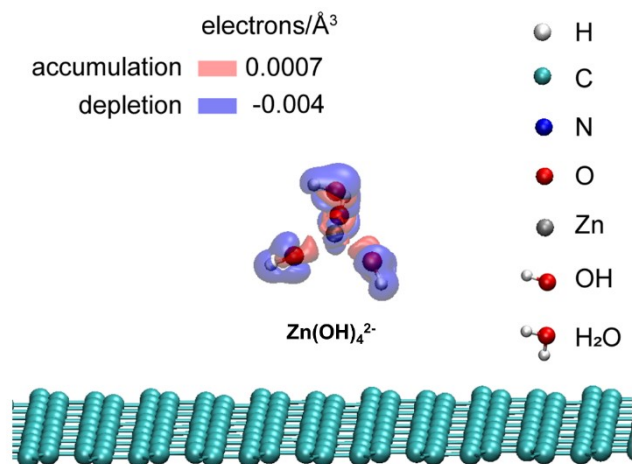


**Fig.S16** Charge density difference (electrons Å<sup>3</sup>) of representative configuration of Zn(OH)<sub>4</sub><sup>2-</sup> adsorbed on graphene to indicate the electron density depletion regions (in blue) and accumulation regions (in red) after adsorption.

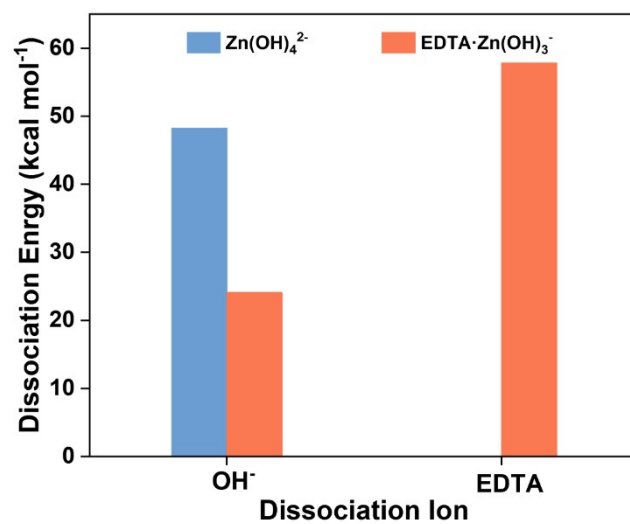


**Fig.S17** The dissociation energy of  $\text{Zn(OH)}_4^{2-}$  and  $\text{EDTA}\cdot\text{Zn(OH)}_3^-$  onto the electrode surface.

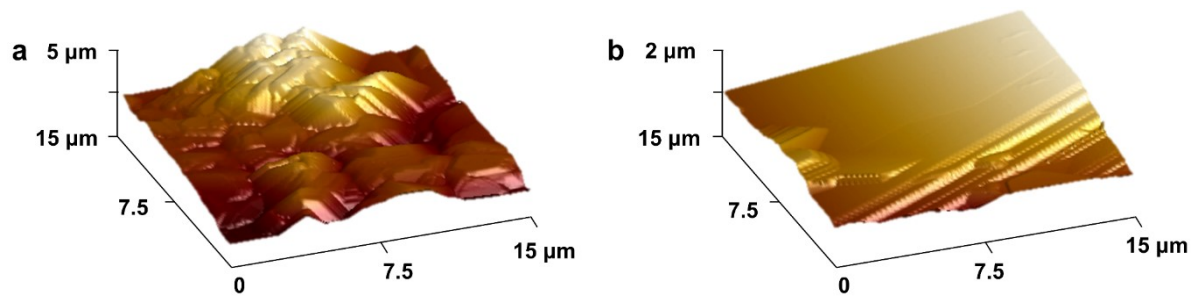


**Fig.S18** In-situ AFM of Zn deposited on electrode at the current density of  $5 \text{ mA cm}^{-2}$  for 700 seconds using (a)  $0.4 \text{ mol L}^{-1} \text{ ZnO}$  +  $3.8 \text{ mol L}^{-1} \text{ OH}^-$  solution, (b)  $0.4 \text{ mol L}^{-1} \text{ ZnO}$  +  $3.8 \text{ mol L}^{-1} \text{ OH}^-$  +  $0.3 \text{ mol L}^{-1} \text{ EDTA}$  solution.

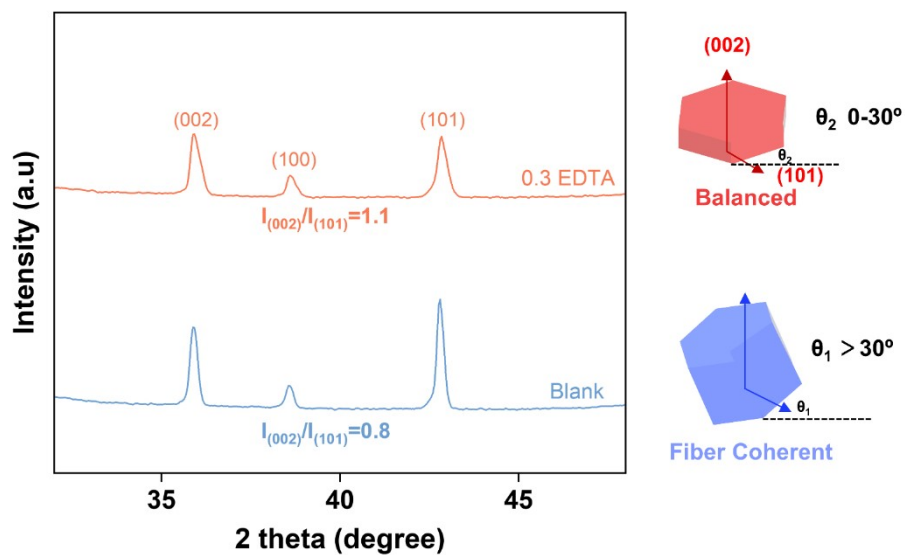


**Fig.S19** XRD patterns of Zn deposited on electrode at the current density of  $5 \text{ mA cm}^{-2}$  for 700 seconds using  $0.4 \text{ mol L}^{-1} \text{ ZnO}$  +  $3.8 \text{ mol L}^{-1} \text{ OH}^-$  without/with  $0.3 \text{ mol L}^{-1} \text{ EDTA}$  solution.

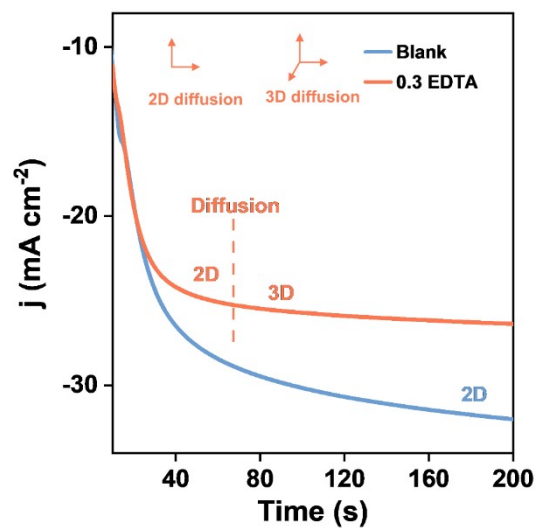


**Fig.S20** The chronoamperograms experiments using  $0.4 \text{ mol L}^{-1} \text{ ZnO} + 3.8 \text{ mol L}^{-1} \text{ OH}^-$  without/with  $0.3 \text{ mol L}^{-1} \text{ EDTA}$  solution in  $\text{Zn} || \text{Zn}$  symmetrical flow battery.

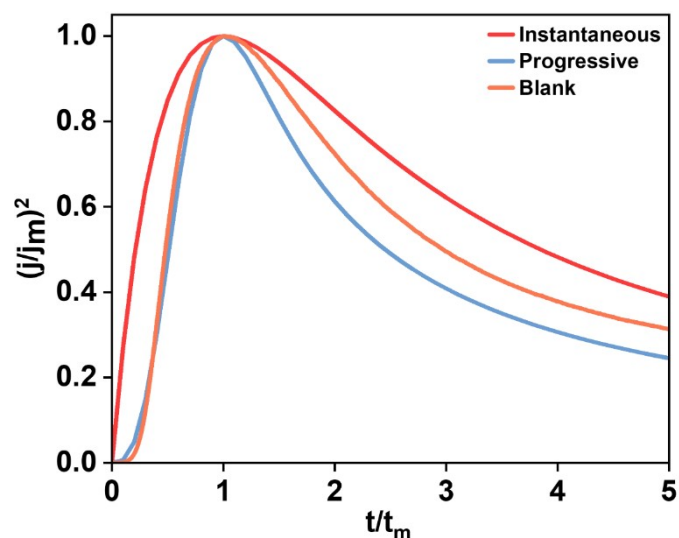


**Fig.S21** Comparison of theoretical dimensionless plots for instantaneous and progressive nucleation to the experimental nucleation process using 0.4 mol L<sup>-1</sup> ZnO + 3.8 mol L<sup>-1</sup> OH<sup>-</sup> solution.

According to the Scharifker model for electrochemical nucleation, nucleation occurs in two distinct forms: instantaneous and progressive<sup>19</sup>. Theoretically, instantaneous nucleation implies that all nuclei emerge at every potential growth site simultaneously during the initial potential step, and subsequently, these nuclei grow at a uniform rate. In contrast, in the progressive nucleation mode, nucleation sites gradually become activated, and the nucleation process is accompanied by the growth of nuclei. The expressions for instantaneous and progressive nucleation are as follows<sup>19</sup>:

Instantaneous:

$$(j/j_m)^2 = 1.9542(t/t_m)^{-1} \{1 - \exp[-1.2564(t/t_m)]\}^2$$

Progressive:

$$(j/j_m)^2 = 1.2254(t/t_m)^{-1} \{1 - \exp[-2.3367(t/t_m)^2]\}^2$$

Where  $j_m$  and  $t_m$  represent the maximal experimental current density and time obtained, respectively. Experimental results and theoretical curves can be compared by plotting the dimensionless parameter  $(j/j_m)^2$  against  $(t/t_m)$ .

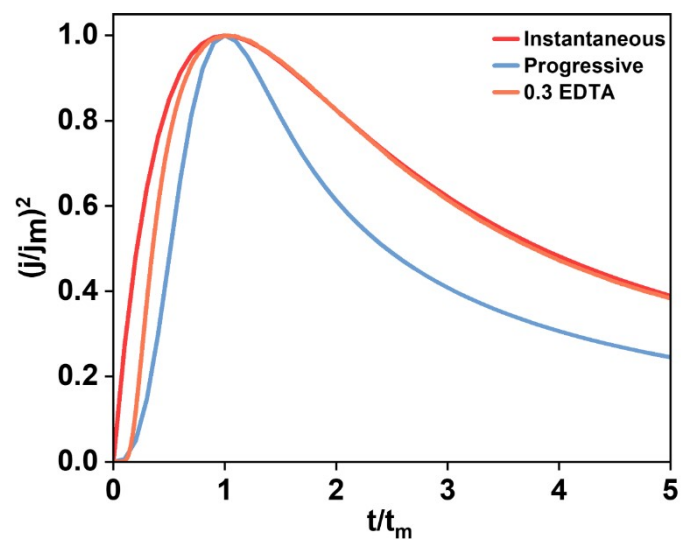


**Fig.S22** Comparison of the theoretical dimensionless plots for instantaneous and progressive nucleation to the experimental nucleation process using 0.4 mol L<sup>-1</sup> ZnO + 3.8 mol L<sup>-1</sup> OH<sup>-</sup> + 0.3 mol L<sup>-1</sup> EDTA solution.

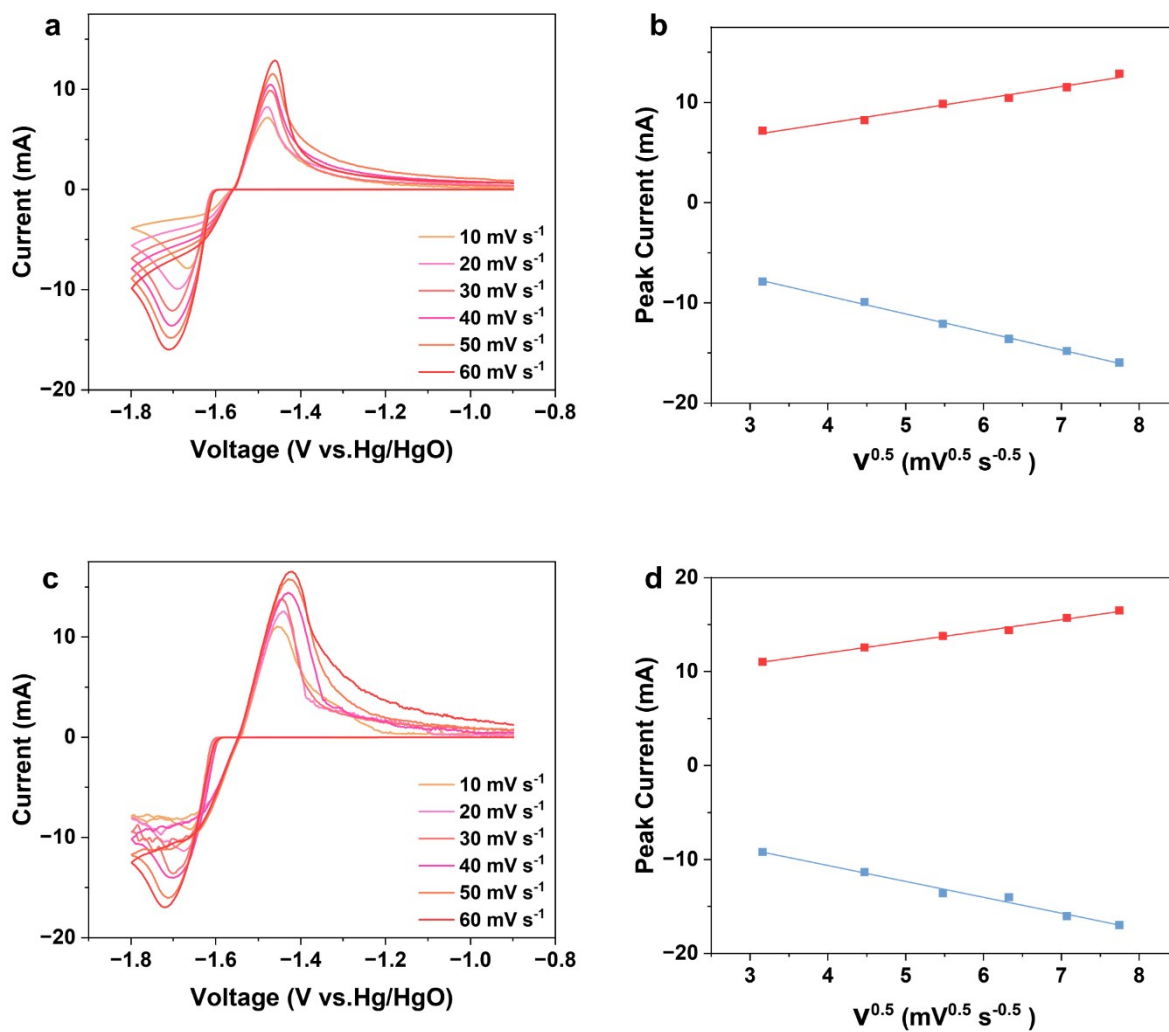


**Fig.S23** (a) Cyclic voltammety (CV) experiment using static solution. (b) Fitted linear of the peak current versus the square root of scanning rates using static solution. (c) CV experiment using non-static solution of 200 rpm. (d) Fitted linear of the peak current versus the square root of scanning rates using non-static solution of 200 rpm.  $0.4 \text{ mol L}^{-1} \text{ ZnO} + 3.8 \text{ mol L}^{-1} \text{ OH}^{-} + 0.3 \text{ mol L}^{-1} \text{ EDTA}$  solution was employed.

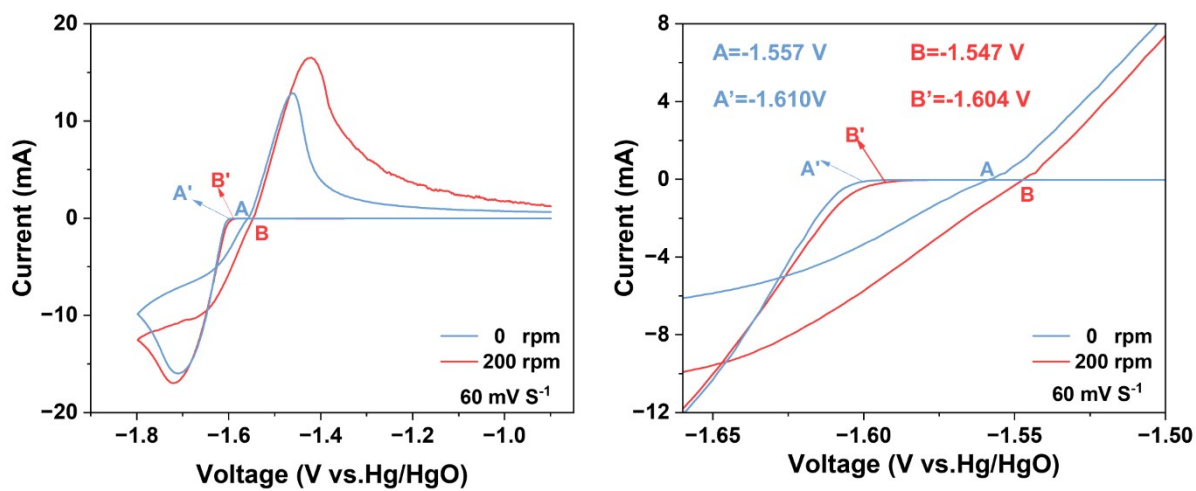


**Fig.S24** CV experiment using static solution and non-static solution at 200 rpm (On the right is an enlarged image).  $0.4 \text{ mol L}^{-1} \text{ ZnO} + 3.8 \text{ mol L}^{-1} \text{ OH}^- + 0.3 \text{ mol L}^{-1} \text{ EDTA}$  solution was employed.

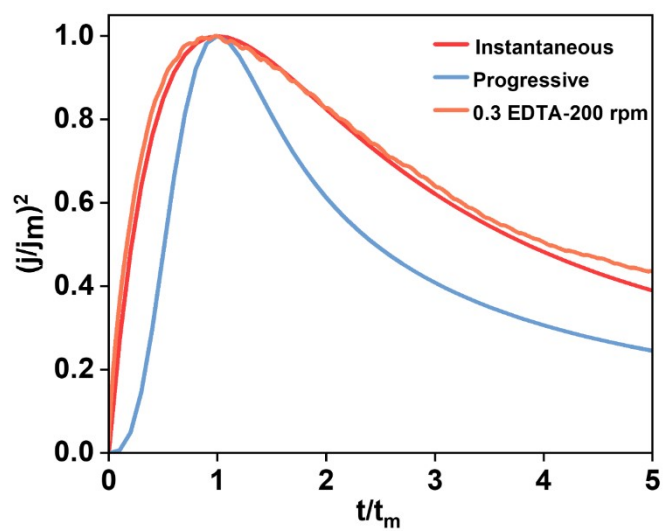


**Fig.S25** Comparison of the theoretical dimensionless plots for instantaneous and progressive nucleation to the experimental nucleation process using non-static solution of  $0.4 \text{ mol L}^{-1} \text{ ZnO} + 3.8 \text{ mol L}^{-1} \text{ OH}^- + 0.3 \text{ mol L}^{-1} \text{ EDTA}$  at 200 rpm.

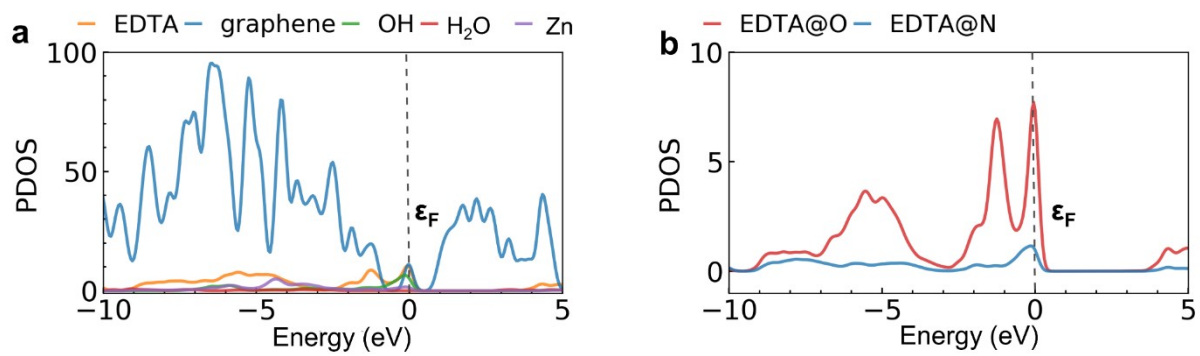


**Fig.S26** PDOS with projections onto EDTA, graphene, OH<sup>-</sup>, H<sub>2</sub>O, and Zn<sup>2+</sup> components for (a) EDTA·Zn(OH)<sub>3</sub><sup>-</sup> on graphene surface and (b) Projections onto atomic orbitals of O and N from EDTA. The Fermi level was set to zero.

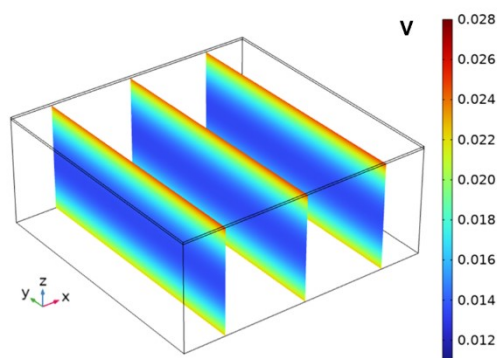


**Fig.S27** The overpotential distribution for battery using  $0.4 \text{ mol L}^{-1} \text{ ZnO} + 3.8 \text{ mol L}^{-1} \text{ OH}^-$  solution (Blank).

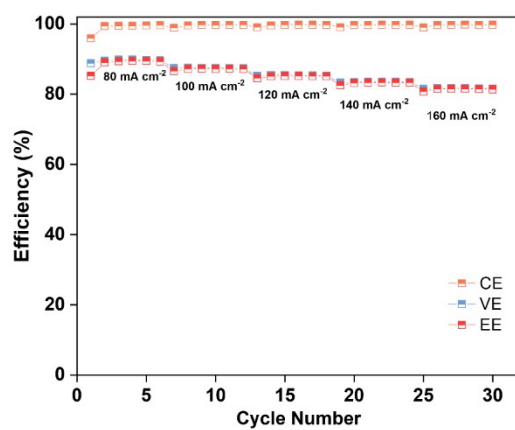


**Fig.S28** The rate performance of AZIFB using 0.4 mol L<sup>-1</sup> ZnO + 3.8 mol L<sup>-1</sup> OH<sup>-</sup> + 0.3 mol L<sup>-1</sup> EDTA solution.

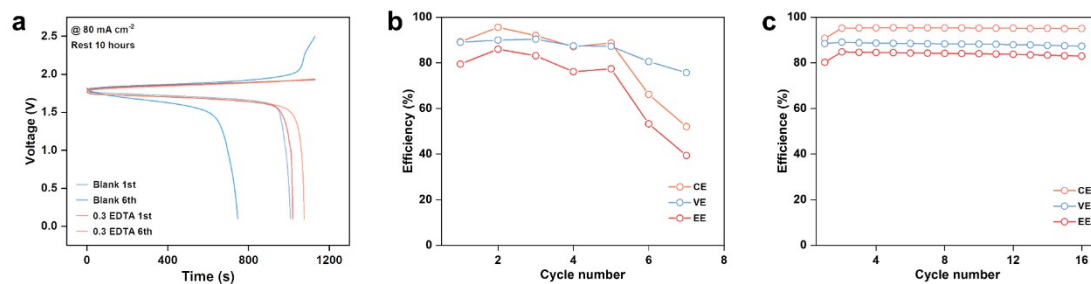


**Fig.S29** The rest performance of AZIFB using 0.4 mol L<sup>-1</sup> ZnO + 3.8 mol L<sup>-1</sup> OH<sup>-</sup> with/without EDTA solution. (a) Voltage-time curves of AZIFB after resting for 10 hours. (b) Efficiency of AZIFB using 0.4 mol L<sup>-1</sup> ZnO + 3.8 mol L<sup>-1</sup> OH<sup>-</sup> without EDTA anolyte. (c) Efficiency of AZIFB using 0.4 mol L<sup>-1</sup> ZnO + 3.8 mol L<sup>-1</sup> OH<sup>-</sup> with 0.3 EDTA anolyte.

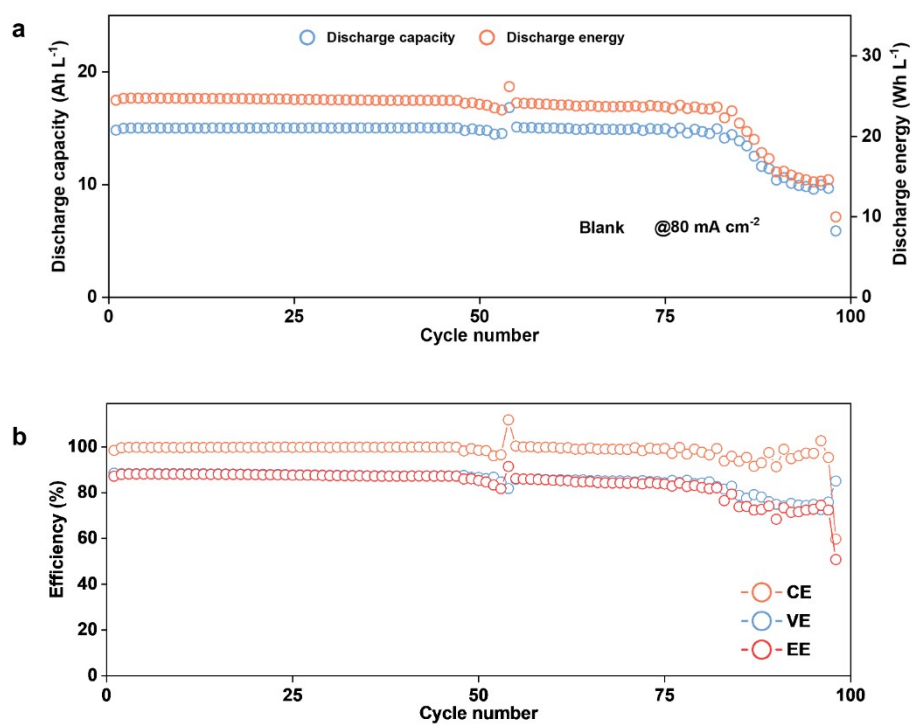


**Fig.S30** The (a) discharge capacity (energy) and (b) cycling performance of AZIFB using 0.4 mol L<sup>-1</sup> ZnO + 3.8 mol L<sup>-1</sup> OH<sup>-</sup> solution.

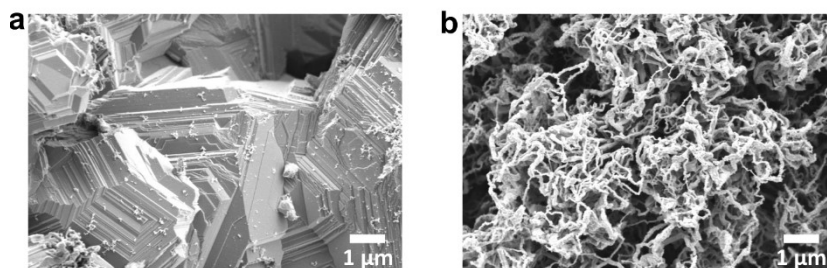


**Fig.S31** The morphology of zinc deposited on anode at the end charging of AZIFB at the current density of  $80 \text{ mA cm}^{-2}$  using  $0.4 \text{ mol L}^{-1} \text{ ZnO} + 3.8 \text{ mol L}^{-1} \text{ OH}^-$  solution (a) with  $0.3 \text{ mol L}^{-1} \text{ EDTA}$ , and (b) without EDTA.

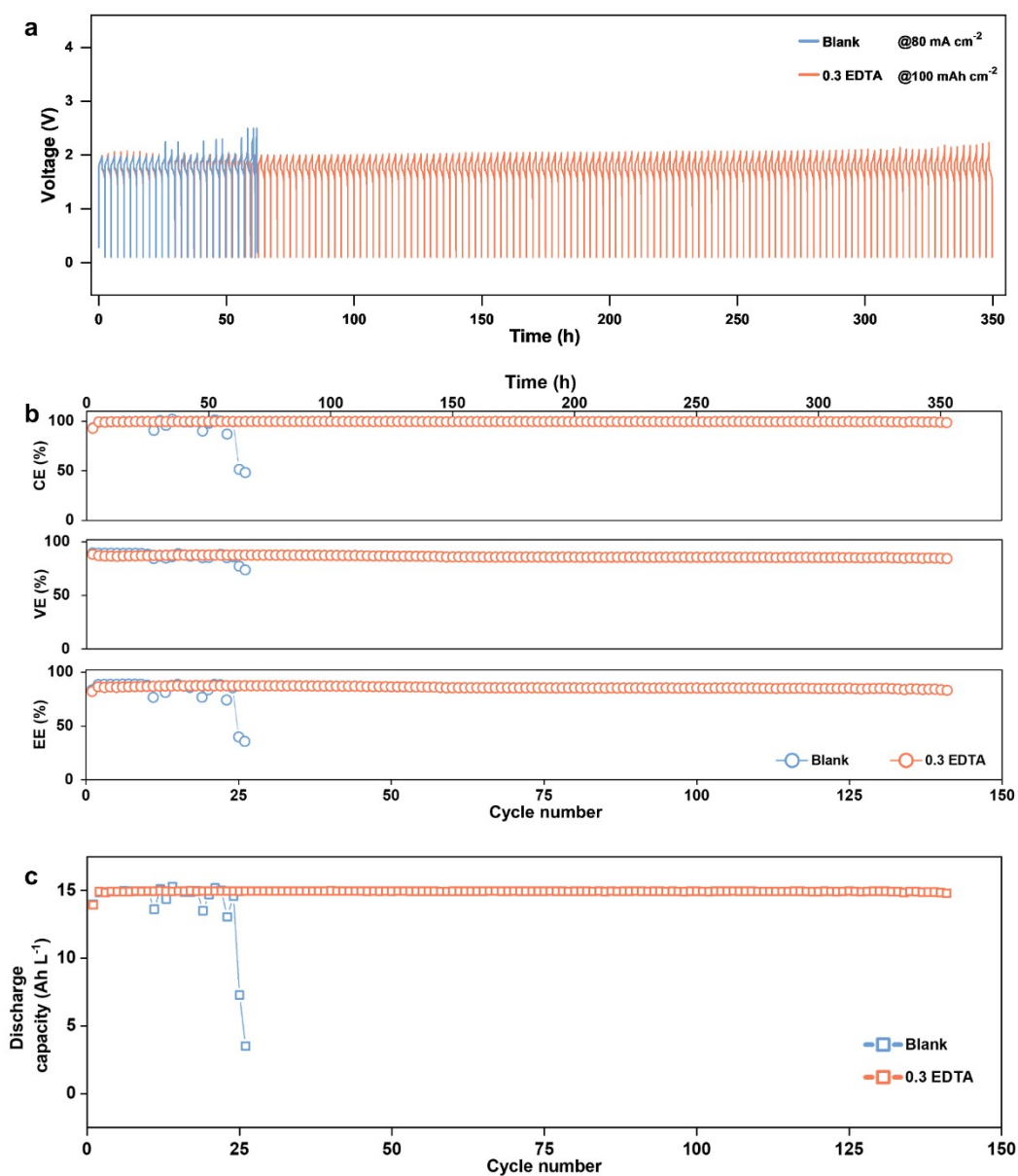


**Fig.S32** The cycling performance with high areal capacity of 100 mAh cm<sup>-2</sup> for AZIFB in 0.4 mol L<sup>-1</sup> ZnO+ 3.8 mol L<sup>-1</sup> OH<sup>-</sup> without/with 0.3 mol L<sup>-1</sup> EDTA. (a) Voltage-time profiles at the current density of 80 mA cm<sup>-2</sup>. (b), (c) The corresponding efficiency and discharge capacity for each cycle, respectively.

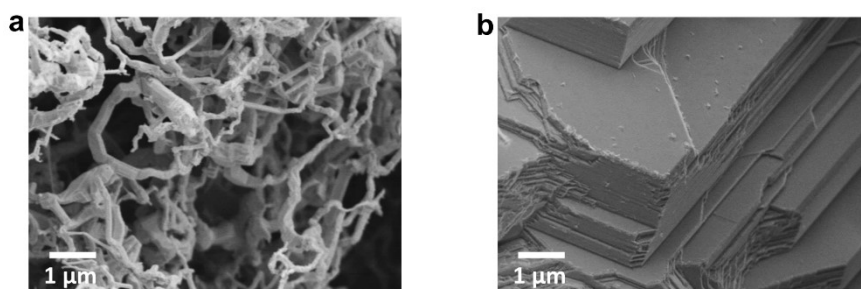


**Fig.S33** The morphology of zinc deposited on anode at the end charging at current density of  $80 \text{ mA cm}^{-2}$  with an areal capacity of  $100 \text{ mAh cm}^{-2}$  for AZIFB using  $0.4 \text{ mol L}^{-1} \text{ ZnO} + 3.8 \text{ mol L}^{-1} \text{ OH}^-$  solution (a) without EDTA, and (b) with  $0.3 \text{ mol L}^{-1} \text{ EDTA}$ .

## Reference

1. L. L. Zhizhang Yuan, Qing Dai, Huamin Zhang, Guangjin Hou, Xianfeng Li, *Joule*, 2022, **6**, 884-905.
2. Y.-S. S. Jeou-Long Lee, *J Chinese Chemical Soc*, 1990, **37**, 265-271.
3. A. Salimi, C. E. Banks and R. G. Compton, *Phys. Chem. Chem. Phys.*, 2003, **5**, 3988-3993.
4. E. J. F. Dickinson and A. J. Wain, *J. Electroanal. Chem.*, 2020, **872**.
5. J. Wang, R. M. Wolf, J. W. Caldwell, P. A. Kollman and D. A. Case, *J. Comput. Chem.*, 2004, **25**, 1157-1174.
6. G. W. T. M. J. Frisch, H. B. Schlegel, G. E. Scuseria, J. R. C. M. A. Robb, G. Scalmani, V. Barone, B. Mennucci, H. N. G. A. Petersson, M. Caricato, X. Li, H. P. Hratchian, J. B. A. F. Izmaylov, G. Zheng, J. L. Sonnenberg, M. Hada, K. T. M. Ehara, R. Fukuda, J. Hasegawa, M. Ishida, T. Nakajima, O. K. Y. Honda, H. Nakai, T. Vreven, J. A. Montgomery, Jr., F. O. J. E. Peralta, M. Bearpark, J. J. Heyd, E. Brothers, V. N. S. K. N. Kudin, R. Kobayashi, J. Normand, A. R. K. Raghavachari, J. C. Burant, S. S. Iyengar, J. Tomasi, N. R. M. Cossi, J. M. Millam, M. Klene, J. E. Knox, J. B. Cross, C. A. V. Bakken, J. Jaramillo, R. Gomperts, R. E. Stratmann, A. J. A. O. Yazyev, R. Cammi, C. Pomelli, J. W. Ochterski, K. M. R. L. Martin, V. G. Zakrzewski, G. A. Voth, J. J. D. P. Salvador, S. Dapprich, A. D. Daniels, J. B. F. O. Farkas, J. V. Ortiz, J. Cioslowski, and a. D. J. Fox, *Journal*, 2009.
7. L. Martínez, R. Andrade, E. G. Birgin and J. M. Martínez, *J. Comput. Chem.*, 2009, **30**, 2157-2164.
8. D. A. Case, I. Y. Ben-Shalom, S. R. Brozell, D. S. Cerutti, T. E. C. III, V. W. D. Cruzeiro, T. A. Darden, R. E. Duke, D. Ghoreishi, M. K. Gilson, H. Gohlke, A. W. Goetz, D. Greene, R. Harris, N. Homeyer, S. Izadi, A. Kovalenko, T. Kurtzman, T. S. Lee, S. LeGrand, P. Li, C. Lin, J. Liu, T. Luchko, R. Luo, D. J. Mermelstein, K. M. Merz, Y. Miao, G. Monard, C. Nguyen, H. Nguyen, I. Omelyan, A. Onufriev, F. Pan, R. Qi, D. R. Roe, A. Roitberg, C. Sagui, S. Schott-Verdugo, J. Shen, C. L. Simmerling, J. Smith, R. Salomon-Ferrer, J. Swails, R. C. Walker, J. Wang, H. Wei, R. M. Wolf, X. Wu, L. Xiao, D. M. York and P. A. Kollman, *AMBER 2018*, University of California, San Francisco, 2018.
9. D. Roe and T. Cheatham, *J. Chem. Theory Comput.*, 2013, **9**, 3084-3095.
10. J. Hunter, *Comput. Sci. Eng.*, 2007, **9**, 90-95.
11. A. Minoia, L. Chen, D. Beljonne and R. Lazzaroni, *Polymer*, 2012, **53**, 5480-5490.
12. H. J. C. Berendsen, D. Vandespoel and R. Vandrungen, *Comput. Phys. Commun.*, 1995, **91**, 43-56.
13. T. Darden, D. York and L. Pedersen, *J. Chem. Phys.*, 1993, **98**, 10089-10092.
14. T. D. Kühne, M. Iannuzzi, M. Del Ben, V. V. Rybkin, P. Seewald, F. Stein, T. Laino, R. Z. Khaliullin, O. Schütt, F. Schiffmann, D. Golze, J. Wilhelm, S. Chulkov, M. H. Bani-Hashemian, V. Weber, U. Borštnik, M. Taillefumier, A. S. Jakobovits, A. Lazzaro, H. Pabst, T. Müller, R. Schade, M. Guidon, S. Andermatt, N. Holmberg, G. K. Schenter, A. Hehn, A. Bussy, F. Belleflamme, G. Tabacchi, A. Glöß, M. Lass, I. Bethune, C. J. Mundy, C. Plessl, M. Watkins, J. VandeVondele, M. Krack and J. Hutter, *The Journal of Chemical Physics*, 2020, **152**, 194103.
15. J. VandeVondele, M. Krack, F. Mohamed, M. Parrinello, T. Chassaing and J. Hutter, *Comput. Phys. Commun.*, 2005, **167**, 103-128.
16. S. Goedecker, M. Teter and J. Hutter, *Physical Review B*, 1996, **54**, 1703-1710.
17. J. P. Perdew, K. Burke and M. Ernzerhof, *Phys. Rev. Lett.*, 1996, **77**, 3865-3868.
18. S. Grimme, J. Antony, S. Ehrlich and H. Krieg, *J. Chem. Phys.*, 2010, **132**, 154104.
19. R. O. B. G. Trejo, Y. Mecis V. P. Ozil, E. Chainet, and B. Nguyen, *J. Electrochem. Soc.*, 1998, **145**, 4090-4097.